processes

MDPI

Article

Photocatalytic Degradation of Azo Dyes in Aqueous Solution Using TiO_2 Doped with rGO/CdS under UV Irradiation

Sunith B. Madduri [1] **and Raghava R. Kommalapati** [1,2,*]

[1] Center for Energy and Environmental Sustainability, Prairie View A&M University, Prairie View, TX 77446, USA; sbmadduri@pvamu.edu
[2] Department of Civil and Environmental Engineering, Prairie View A&M University, Prairie View, TX 77446, USA
* Correspondence: rrkommalapati@pvamu.edu; Tel.: +1-(936)-261-1660

Abstract: Photocatalysis, mainly using TiO_2 as a catalyst, has emerged as a promising method to address the issue of wastewater treatment. This study explores the enhanced photocatalytic activity of TiO_2 through the introduction of reduced graphene oxide (rGO) and cadmium sulfide (CdS) as selective metal dopants. The incorporation of rGO and CdS into the TiO_2 lattice aims to optimize its photocatalytic properties, including bandgap engineering, charge carrier separation, and surface reactivity. The unique combination of CdS and rGO with TiO_2 is expected to boost degradation efficiency and reduce the reliance on expensive and potentially harmful sensitizers. This experimental investigation involves the synthesis and characterization of TiO_2-based photocatalysts. The photocatalytic degradation of methyl orange (MO) and methylene blue (MB) was assessed under controlled laboratory conditions, studying the influence of metal dopants on degradation kinetics and degradation efficiency. Furthermore, the synthesized photocatalyst is characterized by advanced techniques, including BET, SEM, TEM, XRD, and XPS analyses. The degraded samples were analyzed by UV-Vis spectroscopy. Insights into the photoexcitation and charge transfer processes shed light on the role of metal dopants in enhancing photocatalytic performance. The results demonstrate the potential of a TiO_2-rGO-CdS-based photocatalyst in which 100% degradation was achieved within four hours for MO and six hours for MB, confirming efficient azo dye degradation. The findings contribute to understanding the fundamental principles underlying the photocatalytic process and provide valuable guidance for designing and optimizing advanced photocatalytic systems. Ultimately, this research contributes to the development of sustainable and effective technologies for removing azo dyes from various wastewaters, promoting environmental preservation and human well-being.

Keywords: photocatalysis; organic dyes; TiO_2; reduced graphene oxide; CdS; organic pollutant removal

Citation: Madduri, S.B.; Kommalapati, R.R. Photocatalytic Degradation of Azo Dyes in Aqueous Solution Using TiO_2 Doped with rGO/CdS under UV Irradiation. *Processes* **2024**, *12*, 1455. https://doi.org/10.3390/pr12071455

Academic Editor: Belkis Sulbarán Rangel

Received: 17 June 2024
Revised: 9 July 2024
Accepted: 10 July 2024
Published: 12 July 2024

1. Introduction

One of the most significant environmental concerns related to water pollution is the contamination of organic dyes. Around 280,000 tons of industrial effluent containing textile dyes are annually discharged globally into the environment [1]. Improper disposal of dye-containing wastewater from industries can contaminate rivers, lakes, and groundwater. Dyes, especially synthetic ones, can persist in water bodies for a long time, disrupting aquatic ecosystems and affecting aquatic life. Some dyes also contain heavy metals such as mercury, chromium, cadmium, lead, and arsenic as additives [2], which can leach into water, posing additional risks [3]. Azo dyes, also called synthetic organic dyes, contain one or more azo groups (–N=N–) as chromophores commonly used in various applications due to their vibrant colors and versatility [4]. Some typical applications of azo dyes are the textile industry to color fabrics; the printing and packaging industry for coloring inks, paper, and cardboard; food and beverage products, including candies, desserts, and soft

drinks; and cosmetics and personal care products, such as lipsticks, nail polishes, and hair dyes, to provide vibrant and long-lasting colors. Additionally, they are used in the plastics and polymers industry in coloring plastics, rubber, and polymers [5–8].

However, due to their toxicity, these dyes pose potential health hazards such as skin irritation, allergies, and respiratory problems. In severe cases, these dyes can lead to mutagenicity and carcinogenicity [9,10]. Several studies have reported the presence of azo dyes in various products due to contamination [6]. One example of such contamination was reported in a review published by [11] in Ecotoxicology and Environmental Safety. The study found that a number of water and sediment samples contained high levels of azo dyes, indicating that textile industries were likely responsible for the contamination [11]. A more recent study published in the journal Food and Chemical Toxicology in 2021 found that several food products sold in the USA, including spices, tea, chips, and candy, were contaminated with azo dyes. The study's authors concluded that these dyes in food products could pose a potential health risk to consumers. Regulatory agencies such as the United States Department of Agriculture (USDA), the United States Environmental Protection Agency (USEPA), and the Food and Drug Administration (FDA) have established guidelines to ensure the safe use of azo dyes in various products, especially in the food and beverage industry [12,13].

Removal of azo dyes from industrial wastewater is performed by various methods such as chemical coagulation [14], ultrafiltration [15], ion exchange [16], reverse osmosis [17], and adsorption [18,19] using different adsorbents. In recent years, extensive research has been conducted on photocatalysis due to its potential to be applied economically on a commercial scale [20]. However, there are various types (Zinc Oxide, Metal–Organic Frameworks, Perovskite-Based, Carbon-Based) of photocatalysts, and photocatalytic treatment using TiO_2 nanoparticles has emerged as a promising approach due to their high photocatalytic activity, non-toxicity, and chemical stability [21–26]. However, the wide bandgap and rapid recombination of photogenerated charge carriers limit the efficiency of TiO_2-based photocatalysts [27,28]. To overcome these drawbacks, ternary composites such as TiO_2-rGO-CdS have been investigated for enhanced photocatalytic performance [29,30]. rGO exhibits excellent electrical conductivity, which facilitates the rapid transport of photogenerated electrons. This property is crucial for reducing the recombination rate of electron–hole pairs generated in TiO_2 during photocatalysis. The enhanced electron mobility in rGO ensures that more electrons participate in the reduction reactions, thereby improving the overall photocatalytic efficiency. The integration of rGO with TiO_2 creates a heterojunction that enhances charge separation [31,32]. Electrons can migrate from the conduction band of TiO_2 to rGO, while holes remain in the TiO_2, reducing the recombination and prolonging the lifetime of charge carriers. CdS is a semiconductor with a narrower bandgap (~2.4 eV) compared to TiO_2 (3.2 eV), allowing it to absorb visible light more effectively [29–31]. This property extends the photocatalyst's light absorption spectrum into the visible region, thus utilizing a broader range of the solar spectrum. The incorporation of CdS into TiO_2 enables the composite to harness more solar energy, enhancing its overall photocatalytic activity under visible light irradiation [23,28]. Similar to rGO, CdS also contributes to efficient charge separation when combined with TiO_2. The conduction band of CdS is positioned higher than that of TiO_2, facilitating the transfer of electrons from CdS to TiO_2, thereby reducing recombination rates. This effective separation and transfer of charge carriers enhances the generation of reactive oxygen species, which are critical for the degradation of organic pollutants. The synergistic effects between the composite's TiO_2, rGO, and CdS components enhance the overall photocatalytic performance. The TiO_2-rGO-CdS composite illuminated with UV light (380–400 nm) has demonstrated excellent photocatalytic performance in degrading various organic pollutants present in industrial wastewater, such as dyes, phenolic compounds, and pharmaceuticals [33–35].

In this study, a TiO_2-rGO-CdS-based photocatalytic (TRCP) nanocomposite was prepared and applied for the degradation of two azo dyes, methyl orange (MO) and methylene blue (MB), from an aqueous solution. Figure 1 shows the chemical structure of MO, which

is an anionic dye, and MB, which is a low-molecular-weight aromatic-based cationic dye. The TRCP was characterized by Field Emission Scanning Electron Microscopy (FE-SEM), X-ray photoelectron spectroscopy (XPS), X-ray diffraction (XRD), transmission electron microscopy (TEM), and the N_2 Brunauer–Emmett–Teller (BET)-specific surface area. A batch of degradation experiments was conducted to explore the effects of pH, time, and dye removal. The results were analyzed using ultraviolet–visible spectroscopy (UV-Vis) to determine the degradation rate by measuring the dye's absorbance changes over time.

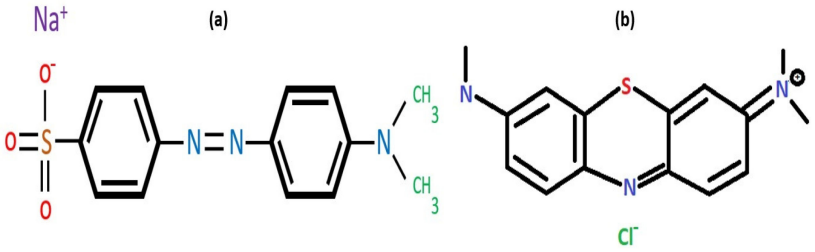

Figure 1. Chemical structure of (**a**) methyl orange and (**b**) methylene blue dyes.

2. Materials and Methods

All the chemicals and reagents used were of analytical grade and purchased from Fisher Scientific, Waltham, MA, USA; Sigma-Aldrich, Saint Louis, MO, USA; and ACS material, Pasadena, CA, USA unless otherwise noted.

2.1. Preparation of Photocatalyst

The TiO_2 nanomaterial was synthesized using the electrochemical anodization method. Anodization, also referred to as anodic oxidation, is an electrochemical process that creates a decorative oxide or protective layer over a metal surface and typically increases the thickness and density of the natural oxide layer that forms, making it more durable and corrosion-resistant. The electrochemical anodization method provides a simple and straightforward approach for synthesizing 1 D TiO_2 nanomaterial using titanium as an anode, a cathode, which is typically a plate of platinum, a DC power supply, and an electrolyte mixture [36,37]. rGO and CdS are two reactants utilized to produce the tri-component photocatalyst [38]. Using the electrochemical anodization method illustrated by [38], titanium foil is first cleaned in a soap solution. The cleaned titanium foil is then ultrasonicated in a mixture containing acetone, isopropyl alcohol, and deionized (DI) water with equal volumes of 50 mL for 30 min before being dried under a nitrogen stream. The electrochemical anodization approach was utilized after the ultrasonication and drying of the titanium foil.

An electrolyte mixture containing 96 mL of diethylene glycol ($C_4H_{10}O_3$) and 0.645 g of ammonium bi-fluoride salt (NH_4HF_2) was used to electrochemically anodize the titanium foil. The prepared titanium foil served as the anode for the anodization setup, and a thin platinum foil served as the cathode. The titanium foil was then anodized at a constant voltage of 25 V for four hours at room temperature while being kept under continuous stirring conditions using a magnetic stirrer. After the anodization, the titanium foil was removed from the sample and rinsed in 2-propanol ($(CH_3)_2CHOH$) and DI water multiple times to remove any debris before being left to dry for one hour. The titanium foil was then annealed at 500 °C for three hours with heating and cooling rates of 1 °C per minute to obtain the anatase phase [39]. An electrophoretic deposition was employed to deposit the graphene oxide onto the titanium nanomaterial [37]. Electrophoretic deposition coats and applies materials to any electrically conductive surface. The anodized titanium foil served as the anode for this method, and the platinum foil served as the cathode for the setup. A total of 200 mL of DI water and 0.01 g of reduced graphene oxide served as the electrolyte solution for the experiment. A voltage of 25 V was applied between the two electrodes, separated at a distance of 2 cm, for a time interval of two hours. A chemical bath deposition technique was employed to deposit the CdS nanoparticles onto the TiO_2-rGO

composite [40]. The precursor solution used for the chemical bath deposition contained 0.0472 g of cadmium nitrate (Cd $(NO_3)_2$) mixed in 100 mL of DI water. A total of 0.0761 g of thiourea (CH_4N_2S) was added to the mixture before adding 7 mL of ammonium solution (NH_4OH). The annealed TiO_2-rGO composite was immersed in the precursor solution at 70 °C for two hours. The resultant titanium foil was then left to dry at room temperature and then annealed at 400 °C for two hours in order to enhance the adhesion between TiO_2 and CdS and form the TRCP [40,41]. The schematic representation of the preparation of the TRCP is shown in Figure S1.

2.2. Photocatalytic Degradation Experiment

The experimental setup involved a 100 mL beaker positioned on a magnetic stirrer. Illumination was provided by a UV lamp (380–400 nm). The entire setup was enclosed within a wooden box lined externally with aluminum foil to prevent external light interference, as illustrated in Figure S2. Notably, the 30 W UV lamp did not impact the reactor's temperature, eliminating the need for external cooling, a departure from similar setups detailed in previous research [42,43]. The efficiency of photocatalysis was assessed by monitoring the degradation of 20 mL each of a 10 mg/L solution containing MO and MB. This evaluation used the prepared TRCP under specific UV light irradiation conditions over a defined period. Optimum studies were conducted for both dyes at different parameters before finalizing the original values, and each experiment was performed in replicates of three. The ultraviolet spectrophotometer was utilized to measure the degradation of the MO and MB solution after response time; the concentration of the target pollutant was calculated through the calibrated standard curve at wavelengths ~465 nm and ~664 nm (maximum absorption peaks). As Beer–Lambert Law indicates, the color fixation straightforwardly corresponds to the absorbance rate of its retention frequency, which is the hypothetical reason for the quantitative investigation of absorbance spectrophotometry. The removal efficiency of dyes can be calculated by Equation (1).

$$r\% = \frac{C_0 - C_t}{C_0} \times 100\% \quad (1)$$

where r (%) is the degradation rate of contaminant over time t; C_0 (μg/L) is the initial concentration of contaminant in the reaction system; and C_t (μg/L) is the concentration of contaminant in the reaction system at time t.

2.3. Photocatalytic Mechanism

TiO_2 is classified as an n-type semiconductor due to its substantial optical energy bandgap, necessitating excitation with low-wavelength light (~380–420 nm) for involvement in photocatalytic processes [44,45]. When exposed to UV light, the TiO_2 catalyst generates photogenerated electron–hole pairs between its valence band (VB) and conduction band (CB) [46]. Subsequently, these pairs undergo recombination and trapping processes. The formation of these photo-induced species follows a reaction sequence outlined below, including the photoexcitation of TiO_2 [47] (Equation (2)), trapping of electron charge carriers (Equation (3)), trapping of hole charge carriers (h^+) (Equation (4)), and recombination of photogenerated carriers (electron and hole pairs) on the semiconductor surface (Equation (5)). The photocatalytic degradation processes are schematically represented in Figure 2.

$$TiO_2 + hv \rightarrow e^- + h^+ \quad (2)$$

$$e^- (CB) \rightarrow e^-(degradation) \quad (3)$$

$$h^+ (VB) \rightarrow h^+(degradation) \quad (4)$$

$$e^- (degradation) + h^+(degradation) \rightarrow heat \quad (5)$$

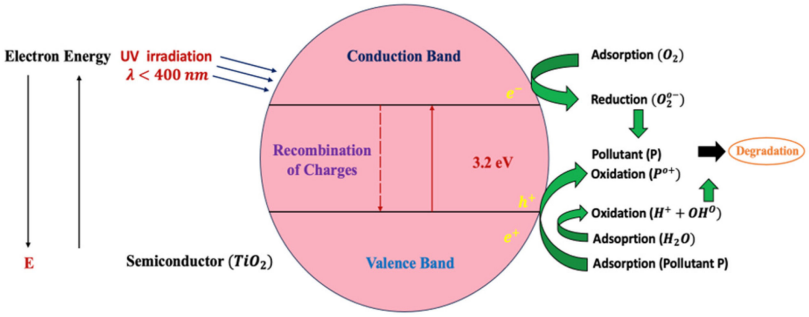

Figure 2. Schematic representation of photocatalytic processes.

2.4. Characterization

The JEOL EDS instrument was used to generate the FE-SEM (JSM-6010LA, JEOL, using InTouch Scope software with version number is 1.11), and the XRD patterns were meticulously analyzed with the Shimadzu 7000 XRD Unit. The N_2 BET adsorption isotherms were analyzed by the NOVA 600 Anton Paar instrument. Each sample was degassed at 300.0 °C at 10.0 °C/min and then held for 180 min before analysis. The degasser employed nitrogen as the adsorbate at a temperature of 77 K while applying the H*e*-mode void volume correction to analyze the isotherms. The Anton Paar Kaomi software for NOVA was utilized. TEM observation was conducted in an aberration-corrected transmission electron microscope (Thermo Fisher Titan Themis Z 300, Houston, TX, USA); the cross-sectional TEM samples were prepared using a Tescan LYRA-3 Model GMH dual-beam focused ion beam (FIB) system; the ion (Ga+) beam operated at 30 kV with a beam current ranging from 12 nA down to 70 pA; the TEM lamella preparation consists of four steps: (1) Pt deposition of a protection layer on the area of interest; (2) milling symmetrical trenches around the lamella and U cut; (3) lift-out using the nanomanipulator and attachment to the TEM grid; and (4) final thinning and cleaning. XPS was measured with the EnviroESCA XPS System; the XPS data were acquired using EnviroESCA with a MonoAl X-ray source with an emission current of 3 mA at a voltage of 14 kV. The Shimadzu UV-1800 UV-Vis spectrophotometer was used to determine the degradation efficiency.

2.5. First-Order Kinetic Model of the Photocatalytic Degradation

The photocatalytic degradation of organic dyes is fitted according to the first-order kinetic model. The first-order kinetic model is proportional to the first power of the reactant concentration. The first-order kinetic expression is as follows [48]:

$$-\frac{dC}{dt} = k \times [\mathrm{C}] \tag{6}$$

$$ln\frac{C_t}{C_0} = -kt \tag{7}$$

$$kt = -\ln(C/C_0) \tag{8}$$

where C_0 is the initial concentration of the dye solution, C_t is the concentration of the reaction at time t (μg/L), and the rate constant (k) is obtained from linear regression analysis of $-\ln(C/C_0)$ with respect to time.

After adjusting the conditions according to the suitable methods described, the photocatalytic degradation of organic dyes was conducted. A first-order kinetic model of the photocatalytic degradation of MO and MB under different reaction conditions was fitted using a linear regression analysis of $-\ln(C/C_0)$ against time t.

3. Results and Discussion

3.1. Characterization of TRCP

The structures of Ti, TiO_2-rGO, and TRCP were investigated using FE-SEM, as depicted in Figure 3a–c. In contrast to the flat surface of Ti (Figure 3c), upon the introduction of

rGO as a loading material, substantial changes occurred in the surface morphology and texture of TiO_2-rGO, resulting in the formation of multileg nanotubes, reaffirming the reliability and robustness of the electrophoretic deposition method as observed in Figure 3a. Importantly, Figure 3b provides strong evidence of the successful loading of CdS onto the surface of the multileg nanotubes, confirming the deposition of CdS onto the surface of TiO_2-rGO. This successful loading reassures us of the effectiveness of our process. The EDS of the TRCP confirms the presence of C, Ti, O, and Cd (Figure 3d).

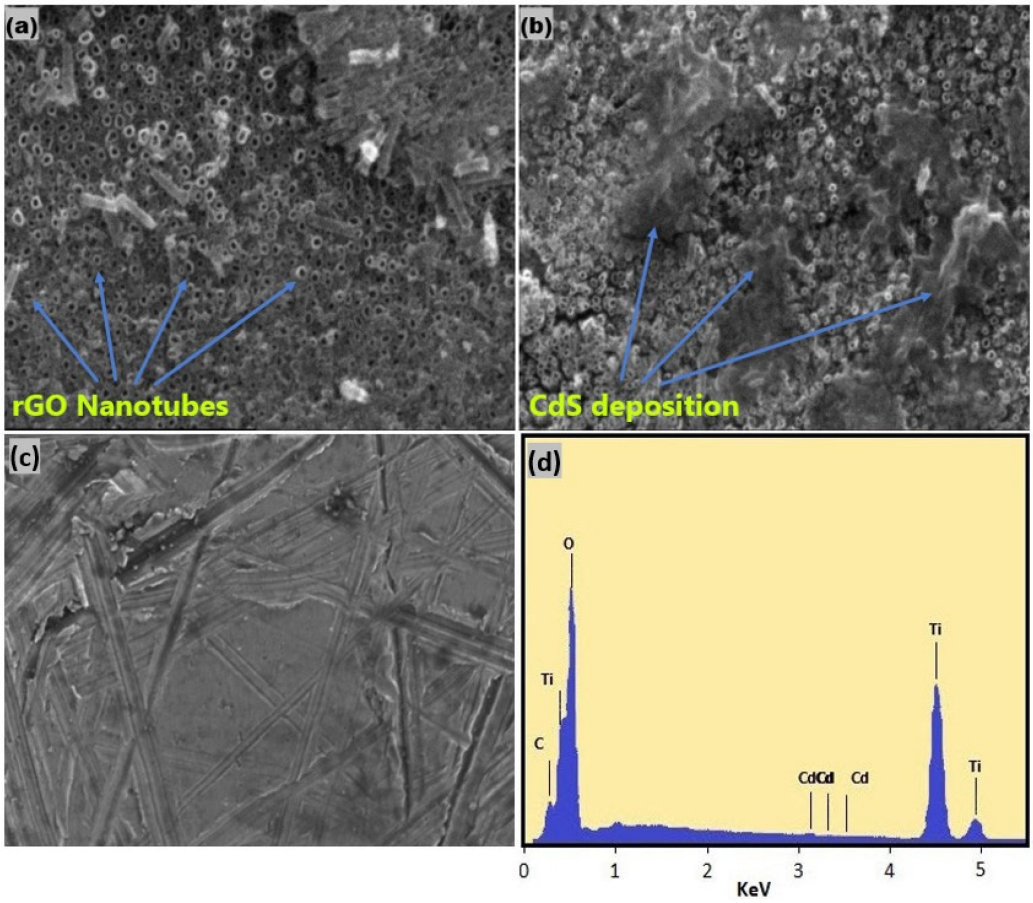

Figure 3. (**a**–**c**) FE-SEM micrographs of TiO_2rGO, TRCP, and Ti; (**d**) EDS spectra of TRCP.

The crystallinity and phase purity of the samples were examined using XRD patterns (Figure 4). The XRD of the TRCP exhibited distinct peaks at 24.75°, 26.3°, 31.1°, 36.6°, 37.5°, 41°, 43.58°, 54.8°, 63.2°, 72.37°, and 75.39°. Among these peaks, those at 36.6° and 54.8° are ascribed to the (101) and (211) planes of the rutile TiO_2 phase (JCPDS Card no. 21-1276), and the peak at 26.3° (002) reflects the rGO phase (JCPDS Card no. 75-2078), indicating the presence of rGO [49]. After deposition of CdS, the characteristic peaks of the nanocomposite are observed at peaks 24.75°, 26.44°, 43.58°, and 75.39°, which can be indexed as the (100), (002), (110), and (212) diffraction planes of CdS with a hexagonal structure (JCPDS #75-1545) [50,51]. This XRD analysis provided clear evidence of the structural characteristics of the synthesized photocatalyst.

Figure 5a–e illustrates the XPS analysis to further determine the chemical composition and valence state of various elements in the photocatalyst. The XPS survey spectrum in Figure 5a indicates O1s peaks at binding energy (BE) ranges of (534.4–533.3) eV, (533.1–532.0) eV, and (532.2–530.7) eV, resulting in the presence of (CO_3^{2-}, O–C=O), (O–C), and (C=O) [52]. Figure 5b explains the presence of Ti_{4+} on the photocatalyst, where the binding energy values of Ti 2p are at 464.0 eV and 458.3 eV, respectively [53]. The binding energies for C1s at ranges 289.7–288.4 eV, 287.7–286.4 eV, 285.8–285.3 eV, and 284.7–284.2 eV

(Figure 5c) correspond to -CO2R(H) and CO32–, C=O, C–O, and (C–H, C–C). Figure 5d displays the Cd3d spectrum of the TRCP, where the binding energies at 411.0 eV and 404.3 eV correspond to $Cd3d_{3/2}$ and $Cd3d_{5/2}$ of Cd^{2+}, respectively. Additionally, two peaks observed at 161.8 eV and 160.5 eV are attributed to the binding energies of $S2p_{3/2}$ and $S2p_{1/2}$, indicating the predominant presence of S^{2-} on the sample surface (Figure 5e) [54]. In summary, the XPS analysis results confirm the successful construction of the heterostructure between TiO_2 and CdS after forming rGO nanotubes, which the TEM discussion can further confirm.

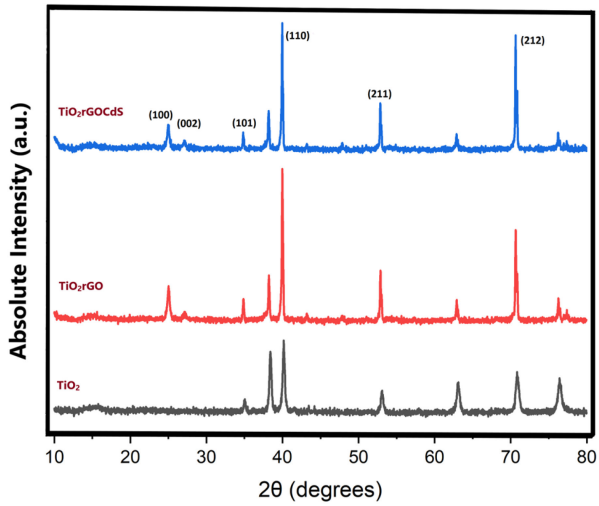

Figure 4. XRD patterns of TiO_2, TiO_2rGO, and TRCP.

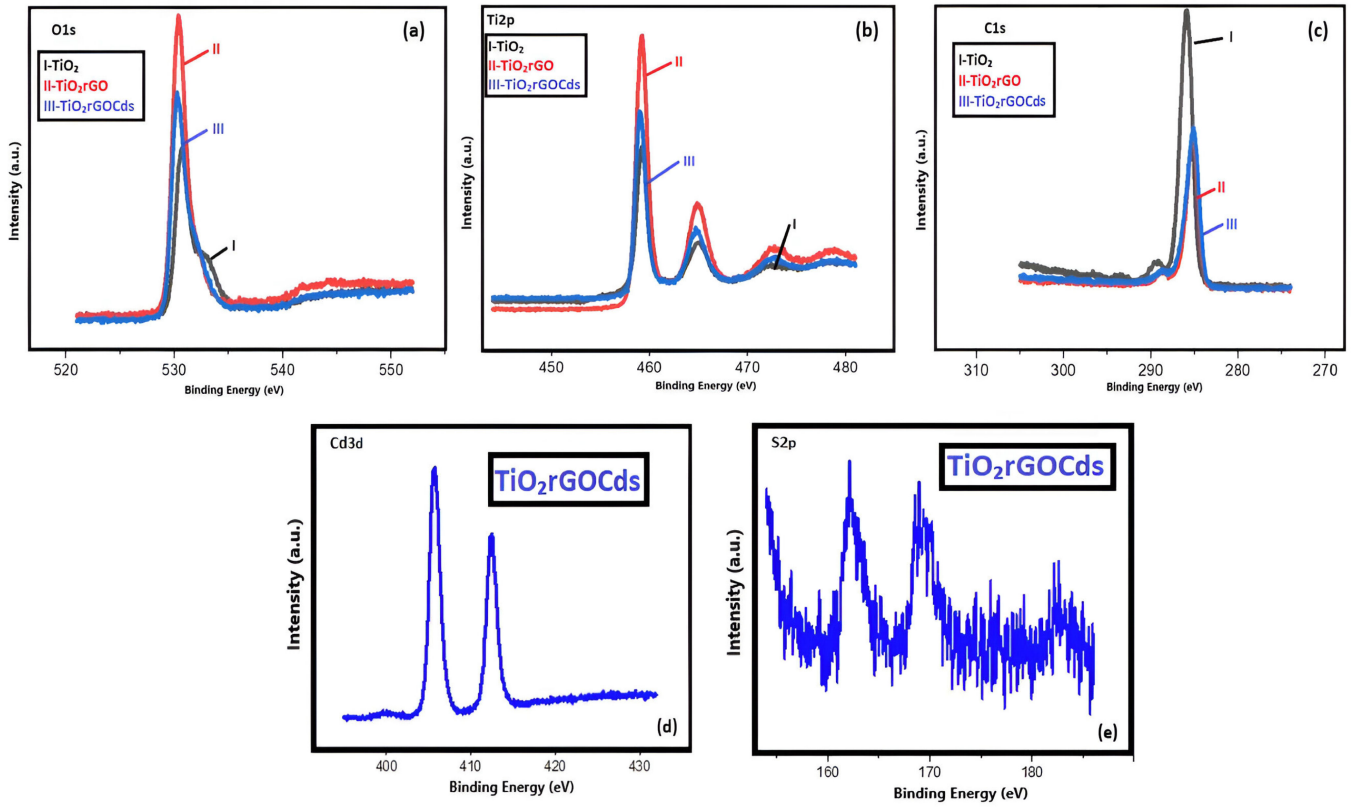

Figure 5. (**a**–**e**) High-resolution (HR) O1s, Ti2p, C1s, Cd3d, and S2p XPS spectra for TiO_2, TiO_2rGO, and TRCP.

TEM imaging shows the development of TiO_2 nanotube embryos and tubes. The nanotubular oxide layer thickness depends linearly on the anodization time, that is, the charge passed during anodization. For stoichiometric titanium dioxide (TiO_2), there are several suboxide phases with fascinating characteristics. These sub-stoichiometric titania compositions can be represented by the general formula Ti_nO_{2n-1} (where $4 \leq n \leq 10$), but certain distinct phases stand out, notably Ti_4O_7, Ti_5O_9, Ti_6O_{11}, Ti_7O_{13}, Ti_8O_{15}, and Ti_9O_{17}. These specific phases are commonly referred to as the Magnéli phases [55]. Element mapping images were generated to display the elemental composition of the surface–near-surface region in the TRCP, revealing well-distributed elements as presented in Figure 6. The TRCP contains C, Cd, N, Ti, and O due to the deposition of CdS. These findings confirm the successful formation of the CdS-TiO_2 heterojunction and the successful incorporation of CdS into the formation of the TRCP. The N_2 BET adsorption isotherm experiment confirmed the specific surface area of the TRCP. The TiO_2rGO sample had an increase in surface area to 0.884 m^2/g from the initial TiO_2 sample of 0.491 m^2/g due to the deposition of rGO. However, the decrease noticed in the TRCP could be due to the deposition of CdS onto the surface. The adsorption/desorption isotherm for the samples indicates a Type IV isotherm, which is characteristic of mesoporous materials. This classification is supported by the presence of a hysteresis loop in the isotherm plots, typically associated with capillary condensation within mesopores. The observed isotherm type and hysteresis loop suggest that the materials possess a mesoporous structure, which is beneficial for photocatalytic applications as it allows for better diffusion and interaction of reactants [51].

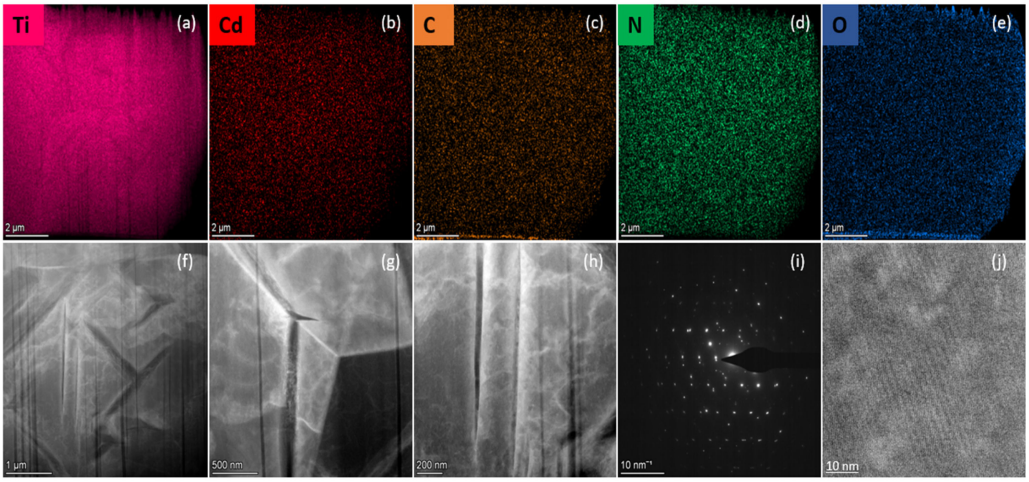

Figure 6. Elemental mapped TEM images and TEM images of TRCP (**a**–**j**).

3.2. Photocatalytic Degradation Study of TRCP

The photocatalytic activity of the TRCP in degrading MO and MB at different pH levels (3, 7, 11) was investigated. The pH of the prepared samples was adjusted with hydrochloric acid (HCl) and sodium hydroxide (NaOH), respectively. The degradation rates of both MO and MB increased initially and eventually plateaued as the reaction progressed. Under acidic conditions, the photocatalytic degradation of MO exhibits exceptional efficiency, a finding with significant implications for our understanding of photocatalysis. The acidic environment likely enhances the TRCP surface charge and promotes the generation of reactive oxygen species (ROS), leading to rapid degradation of MO molecules; the degradation efficiency at pH 3 achieved 100% within 180 min, indicating the robust performance of the photocatalyst in acidic environments for an anionic dye like MO. Contrarily, at pH 11, the photocatalytic degradation of MO is significantly slower compared to acidic conditions, and the alkaline environment might affect the surface properties of the photocatalyst, hindering its ability to generate ROS effectively.

In contrast to MO, MB molecules are also adsorbed onto the surface of the TRCP; at pH 11, the surface of the photocatalyst carries a negative charge due to the alkaline

environment. This electrostatic attraction enhances the adsorption of the cationic MB molecules. When illuminated with UV light, the TRCP generates electron–hole pairs. In an alkaline environment (pH 11), the generation of hydroxyl radicals (•OH) is favored due to the presence of abundant hydroxide ions (OH^-); the degradation efficiency surpasses 100% within 220 min. In acidic solutions (pH 3), the degradation process of MB was hindered due to the abundance of protons, leading to decreased efficiency. The pH of the solution plays a crucial role in determining the surface charge of both the photocatalyst and the organic dye molecules. This surface charge affects the adsorption of the dye molecules onto the catalyst and the generation of reactive oxygen species, thereby influencing the efficiency of the photocatalytic degradation process (Figure 7a,b). Additional experiments were conducted to explore the impact of different temperatures (10, 25, and 40 °C) on the photodegradation rates of MO and MB. Graphs depicting degradation percentages over time within the temperature range of 10 to 40 °C are presented in Figure 7c,d. The removal efficiencies of both MO and MB remained relatively consistent across different temperatures. The subtle increase in the degradation rates could be attributed to the endothermic nature of the degradation process, indicating a nuanced relationship between temperature and the overall photodegradation kinetics. This finding underscores the fact that the photocatalytic process can maintain its effectiveness even when the temperature changes, highlighting its adaptability across varying temperature conditions. Photocatalytic degradation of MO and MB was conducted at different time intervals ranging from 30 min to 24 h, with measurements taken at 1 h intervals. Figure 8a,b illustrate the maximum degradation percentages of both dyes at 240 min and 360 min, respectively, under pH 7 conditions similar to natural water.

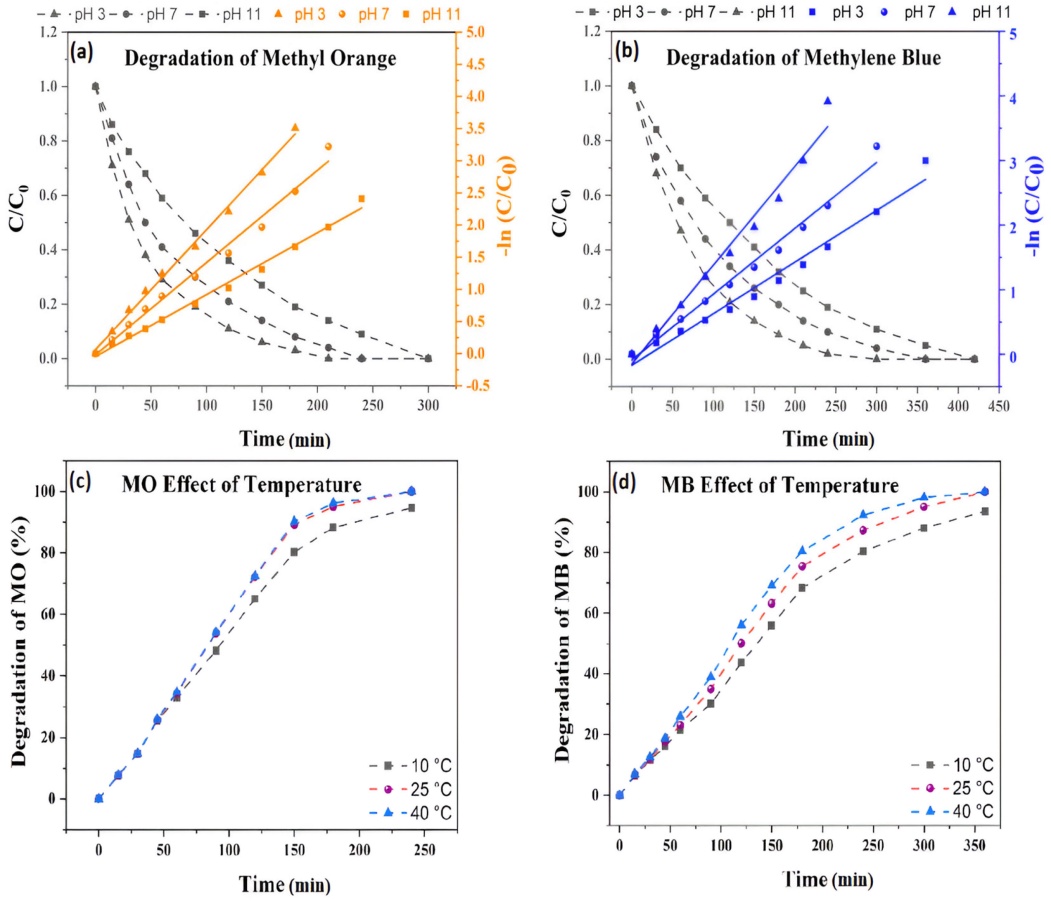

Figure 7. (**a**,**b**) Effect of pH on the photocatalytic degradation of MO and MB; (**c**,**d**) effect of temperature on the photocatalytic degradation of MO and MB at pH 7.

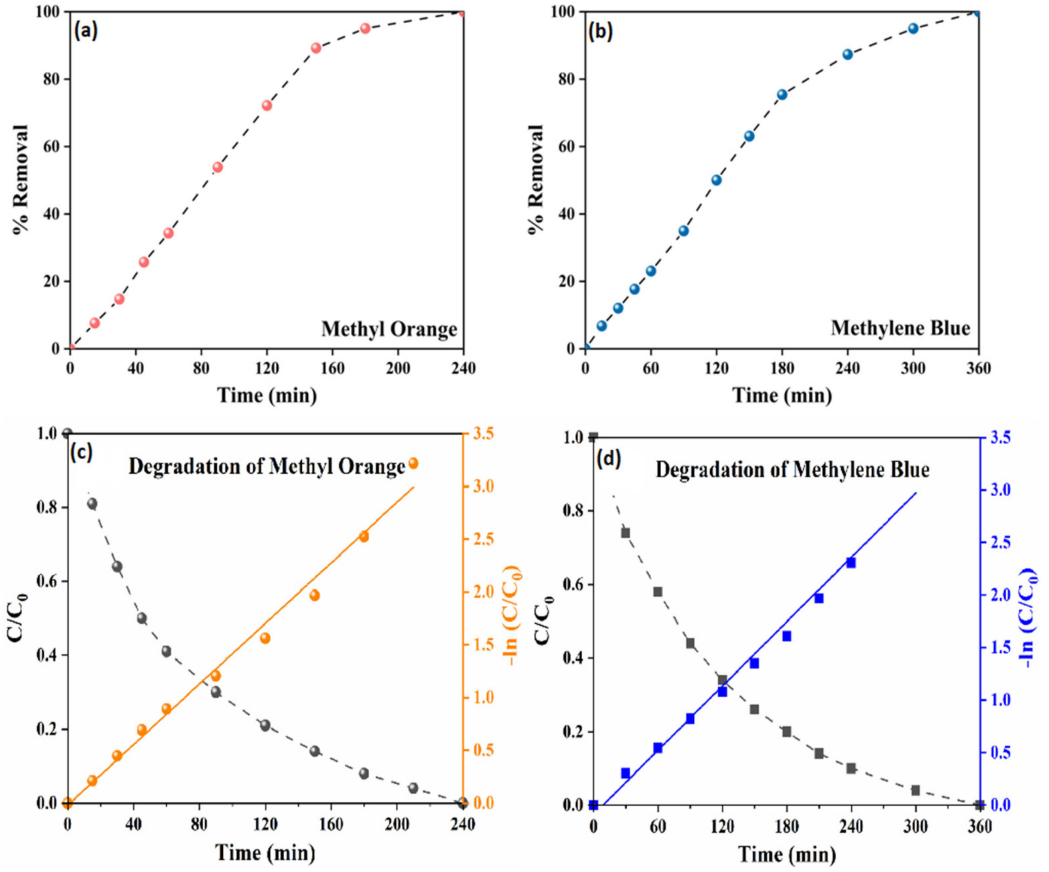

Figure 8. (**a**,**b**) Removal percentage behavior of photocatalytic degradation of MO and MB over time (**c**,**d**) first-order kinetic model of photocatalytic degradation (C/C_0) and $-\ln(C/C_0)$ against time for MO and MB.

3.3. Photocatalytic Mechanism of TRCP

In the photocatalytic reaction, CdS (bandgap energy, Eg = 2.4 eV) acts as a sensitizer, effectively absorbing photons from visible light and exciting electrons in the valence band. These excited electrons are then captured by TiO_2 (bandgap energy, Eg = 3.2 eV) from CdS nanoparticles. However, the unique properties of rGO make it crucial as a mediator, transporter, and sensitizer for degrading organic pollutants between TiO_2 and CdS nanoparticles. Its exceptional ability to facilitate charge separation, transfer, and light absorption sets it apart. Within the TRCP composite, rGO acts as an electron transfer medium, efficiently shuttling photogenerated electrons and channeling them to TiO_2. This extended electron transport path reduces hindrance and minimizes charge recombination.

Furthermore, rGO serves as a protective barrier, shielding CdS nanoparticles from photocorrosion like a reliable, protective blanket. When exposed to radiation with energy equal to or greater than the energy gap, electrons from the lower-energy valence band of CdS are excited to the high-energy conduction band of TiO_2, generating highly reactive electrons and holes. These photoelectrons possess higher energy levels and are highly reactive with solid oxidation capabilities, while the holes (h+) capable of accepting electrons from adsorbed species exhibit significant reducibility. Water (H_2O) and oxygen (O_2) molecules adsorbed on the surface of the composite materials react with these electrons and holes, forming potent oxidative radicals such as ·OH and $\cdot O_2$. Subsequent reactions between these radicals and pollutants lead to the degradation of pollutants into smaller molecules. The large surface area and electrical conductivity of rGO enhance the transmission efficiency of charge carriers on the composite material's surface, reducing the likelihood of electron–hole recombination. This improved efficiency and enhanced light energy utilization contribute to the increased photocatalytic performance of the TRCP. Figure 9 depicts a schematic repre-

sentation of the TRCP photocatalytic mechanism. Figure 8c,d show that the photocatalysis for MO and MB followed the first-order kinetic model, which is described by Equation (8) and can be obtained from the slope of $(-\ln (C/C_0))$ versus time (t), as shown in Table 1.

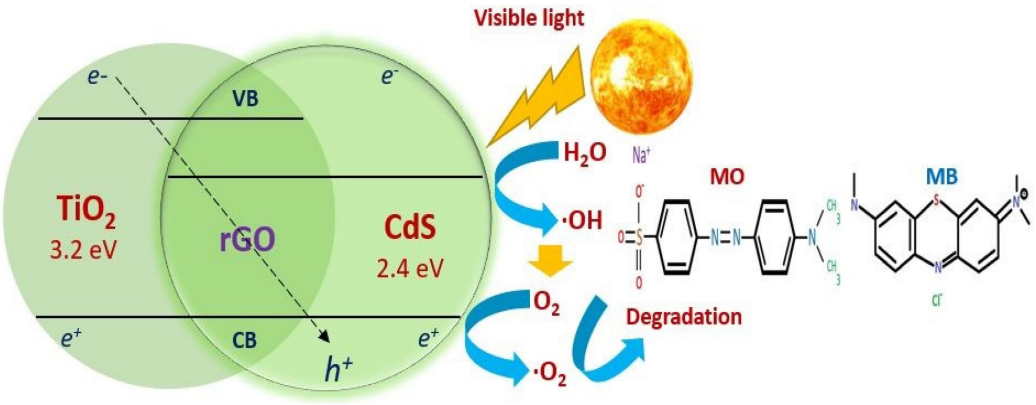

Figure 9. Schematic representation of TRCP photocatalytic mechanism.

Table 1. Kinetic fitting data of MO and MB at pH 7.

Experiments	Reaction Rate Constant (min^{-1})	R-Square (R^2)
MO	0.0143	0.988
MB	0.0101	0.986

Table 2 presents a comparison of the degradation efficiency of the TiO_2 composite with other materials documented in the recent literature. All photocatalytic experiments were conducted under ultraviolet light to maintain consistency across the comparisons. The TRCP displayed reasonable performance compared to the materials listed, demonstrating higher removal rates and efficiency for the MO and MB dye pollutants. These results highlight the competitive edge of the TRCP in the photocatalytic degradation of dyes.

Table 2. Comparison of photocatalytic performance of TiO_2rGOCds photocatalyst with reported literature.

Photocatalyst	Dye	Irradiation Time (min)	Efficiency (%)	Reference
Se-ZnSNCS	MO	160	95.00	[56]
N-TiO_2	MO	200	90.00	[57]
α-Bi_2O_3	MO	150	95.00	[58]
N-TiO_2 nanorods	MO	250	80.00	[59]
α-Fe_2O_3 nanoparticles	MO	100	95.31	[60]
ZnO quantum dots	MO	160	97.00	[61]
ZnO nanopyramid	MO	150	95.00	[62]
Fe–ZnO	MB	180	92	[63]
GO/TiO_2	MB	240	100	[64]
Cd–ZnO	MB	240	89	[65]
Fe_3O_4–ZnO NCS	MB	180	89.2	[66]
N-Carbon quantum dots/TiO_2	MB	420	82.00	[67]
S-TiO_2 nanorods	MB	240	92.00	[68]
Egg-NiO	MB	240	79.00	[69]
TiO_2rGOCdS	MO	240	100	This work
TiO_2rGOCdS	MB	360	100	This work

4. Conclusions

Photocatalysis, mainly using TiO_2 as a catalyst, has emerged as a promising method to address the issue of wastewater treatment. This study explores the enhanced photo-

catalytic activity of TiO_2 through the introduction of reduced graphene oxide (rGO) and cadmium sulfide (CdS) as selective metal dopants. The incorporation of rGO and CdS into the TiO_2 lattice aims to optimize its photocatalytic properties, including bandgap engineering, charge carrier separation, and surface reactivity. The unique combination of CdS and rGO with TiO_2 is expected to boost degradation efficiency and reduce the reliance on expensive and potentially harmful sensitizers. The experimental investigation involves the synthesis and characterization of TiO_2-based photocatalysts. The photocatalytic degradation of methyl orange (MO) and methylene blue (MB) was assessed under controlled laboratory conditions, studying the influence of metal dopants on degradation kinetics and degradation efficiency. Insights into the photoexcitation and charge transfer processes shed light on the role of metal dopants in enhancing photocatalytic performance. The results demonstrate the potential of a TiO_2-rGO-CdS-based photocatalyst in which 100% degradation was achieved within four hours for MO and six hours for MB, confirming efficient azo dye degradation. The findings contribute to understanding the fundamental principles underlying the photocatalytic process and provide valuable guidance for designing and optimizing advanced photocatalytic systems. Ultimately, this research contributes to the development of sustainable and effective technologies for removing azo dyes from various wastewaters, promoting environmental preservation and human well-being.

Supplementary Materials: The following supporting information can be downloaded at https://www.mdpi.com/article/10.3390/pr12071455/s1: Figure S1. Schematic representation of preparation of TRCP; Figure S2. Photocatalytic degradation experimental setup.

Author Contributions: Conceptualization, S.B.M. and R.R.K.; Methodology, S.B.M.; Writing—Original draft preparation, S.B.M.; Funding acquisition, R.R.K.; Supervision, R.R.K.; Reviewing and Editing, R.R.K. All authors have read and agreed to the published version of the manuscript.

Funding: This work was supported by the National Science Foundation (NSF) through the CREST Center for Energy and Environmental Sustainability-Phase II (CEES) (Award #1900857) and with partial support from the NSF Excellence in Research project (Award #1900787).

Data Availability Statement: Data are contained within the article.

Conflicts of Interest: The authors declare no conflicts of interest.

References

1. Zhou, W.; Chen, X.; Ismail, M.; Wei, L.; Hu, B. Simulating the synergy of electron donors and different redox mediators on the anaerobic decolorization of azo dyes: Can AQDS-chitosan globules replace the traditional redox mediators? *Chemosphere* **2021**, *275*, 130025. [CrossRef] [PubMed]
2. Yang, G.; Zhang, G.; Wang, H. Current state of sludge production, management, treatment and disposal in China. *Water Res.* **2015**, *78*, 60–73. [CrossRef] [PubMed]
3. Tkaczyk, A.; Mitrowska, K.; Posyniak, A. Synthetic organic dyes as contaminants of the aquatic environment and their implications for ecosystems: A review. *Sci. Total Environ.* **2020**, *717*, 137222. [CrossRef] [PubMed]
4. Mezgebe, K.; Mulugeta, E. Synthesis and pharmacological activities of azo dye derivatives incorporating heterocyclic scaffolds: A review. *RSC Adv.* **2022**, *12*, 25932–25946. [CrossRef] [PubMed]
5. Cui, D.; Cui, M.-H.; Liang, B.; Liu, W.-Z.; Tang, Z.-E.; Wang, A.-J. Mutual effect between electrochemically active bacteria (EAB) and azo dye in bio-electrochemical system (BES). *Chemosphere* **2020**, *239*, 124787. [CrossRef] [PubMed]
6. Huang, D.; Pozhidaev, E.; Chigrinov, V.; Cheung, H.; Ho, Y.; Kwok, H. Photo-aligned ferroelectric liquid crystal displays based on azo-dye layers. *Displays* **2004**, *25*, 21–29. [CrossRef]
7. Wang, Y.; Bi, N.; Zhang, H.; Tian, W.; Zhang, T.; Wu, P.; Jiang, W. Visible-light-driven photocatalysis-assisted adsorption of azo dyes using Ag_2O. *Colloids Surf. A Physicochem. Eng. Asp.* **2020**, *585*, 124105. [CrossRef]
8. Zhao, B.; Zhu, Z.; Qin, X.D.; Li, Z.; Zhang, H. Highly efficient and stable CuZr-based metallic glassy catalysts for azo dye degradation. *J. Mater. Sci. Technol.* **2020**, *46*, 88–97. [CrossRef]
9. Navarro, A.; Sanz, F. Dye aggregation in solution: Study of C.I. direct red I. *Dye. Pigment.* **1999**, *40*, 131–139. [CrossRef]
10. Ravi, B.N.; Keshavayya, J.; Kumar, V.; Kandgal, S. Synthesis, characterization and pharmacological evaluation of 2-aminothiazole incorporated azo dyes. *J. Mol. Struct.* **2020**, *1204*, 127493. [CrossRef]
11. Al-Tohamy, R.; Ali, S.S.; Li, F.; Okasha, K.M.; Mahmoud, Y.A.-G.; Elsamahy, T.; Jiao, H.; Fu, Y.; Sun, J. A critical review on the treatment of dye-containing wastewater: Ecotoxicological and health concerns of textile dyes and possible remediation approaches for environmental safety. *Ecotoxicol. Environ. Saf.* **2022**, *231*, 113160. [CrossRef]

12. Aigbe, U.O.; Ukhurebor, K.E.; Onyancha, R.B.; Osibote, O.A.; Darmokoesoemo, H.; Kusuma, H.S. Fly ash-based adsorbent for adsorption of heavy metals and dyes from aqueous solution: A review. *J. Mater. Res. Technol.* **2021**, *14*, 2751–2774. [CrossRef]
13. Cruz, D.R.; de Jesus, G.K.; Santos, C.A.; Silva, W.R.; Wisniewski, A.; Cunha, G.C.; Romão, L.P. Magnetic nanostructured material as heterogeneous catalyst for degradation of AB210 dye in tannery wastewater by electro-Fenton process. *Chemosphere* **2021**, *280*, 130675. [CrossRef]
14. Duan, Y.; Zhao, J.; Qiu, X.; Deng, X.; Ren, X.; Ge, W.; Yuan, H. Coagulation performance and floc properties for synchronous removal of reactive dye and polyethylene terephthalate microplastics. *Process Saf. Environ. Prot.* **2022**, *165*, 66–76. [CrossRef]
15. Li, N.; Lou, T.J.; Wang, W.; Li, M.; Jing, L.C.; Yang, Z.X.; Chang, R.Y.; Li, J.; Geng, H.Z. MXene-PANI/PES composite ultrafiltration membranes with conductive properties for anti-fouling and dye removal. *J. Membr. Sci.* **2023**, *668*, 121271. [CrossRef]
16. Kaur, K.; Jindal, R. Comparative study on the behaviour of Chitosan-Gelatin based Hydrogel and nanocomposite ion exchanger synthesized under microwave conditions towards photocatalytic removal of cationic dyes. *Carbohydr. Polym.* **2019**, *207*, 398–410. [CrossRef]
17. An, M.; Gutierrez, L.; D'Haese, A.; Tan, L.; Verliefde, A.; Cornelissen, E. In-situ modification of nanofiltration and reverse osmosis membranes for organic micropollutants and salts removal: A review. *Desalination* **2023**, *565*, 116861. [CrossRef]
18. Navarathna, C.M.; Dewage, N.B.; Karunanayake, A.G.; Farmer, E.L.; Perez, F.; Hassan, E.B.; Mlsna, T.E.; Pittman, C.U., Jr. Rhodamine B Adsorptive Removal and Photocatalytic Degradation on MIL-53-Fe MOF/Magnetic Magnetite/Biochar Composites. *J. Inorg. Organomet. Polym. Mater.* **2020**, *30*, 214–229. [CrossRef]
19. Madduri, S.; Elsayed, I.; Hassan, E.B. Novel oxone treated hydrochar for the removal of Pb(II) and methylene blue (MB) dye from aqueous solutions. *Chemosphere* **2020**, *260*, 127683. [CrossRef]
20. Chandrabose, G.; Dey, A.; Gaur, S.S.; Pitchaimuthu, S.; Jagadeesan, H.; Braithwaite, N.S.J.; Selvaraj, V.; Kumar, V.; Krishnamurthy, S. Removal and degradation of mixed dye pollutants by integrated adsorption-photocatalysis technique using 2-D MoS_2/TiO_2 nanocomposite. *Chemosphere* **2021**, *279*, 130467. [CrossRef]
21. Ahmad, A.; Ali, M.; Al-Sehemi, A.G.; Al-Ghamdi, A.A.; Park, J.-W.; Algarni, H.; Anwer, H. Carbon-integrated semiconductor photocatalysts for removal of volatile organic compounds in indoor environments. *Chem. Eng. J.* **2023**, *452*, 139436. [CrossRef]
22. Aswini, R.; Padmanaban, A.; Vigneshwaran, S.; Valdes, H.; Arunachalam, S. A review on versatile nano-photocatalysts for environmental remediation: Carbon-decorated bismuth-based nanomaterials. *Nano-Struct. Nano-Objects* **2023**, *35*, 100991. [CrossRef]
23. Bibi, S.; Shah, S.S.; Muhammad, F.; Siddiq, M.; Kiran, L.; Aldossari, S.A.; Mushab, M.S.S.; Sarwar, S. Cu-doped mesoporous TiO_2 photocatalyst for efficient degradation of organic dye via visible light photocatalysis. *Chemosphere* **2023**, *339*, 139583. [CrossRef] [PubMed]
24. Ji, Q.; Yan, X.; Xu, J.; Wang, C.; Wang, L. Fabrication of hollow type-II and Z-scheme $In_2O_3/TiO_2/Cu_2O$ photocatalyst based on In-MIL-68 for efficient catalytic degradation of tetracycline. *Sep. Purif. Technol.* **2021**, *265*, 118487. [CrossRef]
25. Sun, P.; Xing, Z.; Li, Z.; Zhou, W. Recent advances in quantum dots photocatalysts. *Chem. Eng. J.* **2023**, *458*, 141399. [CrossRef]
26. Wang, X.; He, J.; Chen, X.; Ma, B.; Zhu, M. Metal halide perovskites for photocatalytic CO_2 reduction: An overview and prospects. *Coord. Chem. Rev.* **2023**, *482*, 215076. [CrossRef]
27. Li, Z.; Wang, S.; Wu, J.; Zhou, W. Recent progress in defective TiO_2 photocatalysts for energy and environmental applications. *Renew. Sustain. Energy Rev.* **2022**, *156*, 111980. [CrossRef]
28. Xu, H.; Yang, J.; Li, Y.; Fu, F.; Da, K.; Cao, S.; Chen, W.; Fan, X. Fabrication of Bi_2O_3 QDs decorated TiO_2/BiOBr dual Z-scheme photocatalysts for efficient degradation of gaseous toluene under visible-light. *J. Alloys Compd.* **2023**, *950*, 169959. [CrossRef]
29. Basavarajappa, P.S.; Patil, S.B.; Ganganagappa, N.; Reddy, K.R.; Raghu, A.V.; Reddy, C.V. Recent progress in metal-doped TiO_2, non-metal doped/codoped TiO_2 and TiO_2 nanostructured hybrids for enhanced photocatalysis. *Int. J. Hydrogen Energy* **2020**, *45*, 7764–7778. [CrossRef]
30. Zhao, Y.; Linghu, X.; Shu, Y.; Zhang, J.; Chen, Z.; Wu, Y.; Shan, D.; Wang, B. Classification and catalytic mechanisms of heterojunction photocatalysts and the application of titanium dioxide (TiO_2)-based heterojunctions in environmental remediation. *J. Environ. Chem. Eng.* **2022**, *10*, 108077. [CrossRef]
31. Azam, M.U.; Tahir, M.; Umer, M.; Tahir, B.; Shehzad, N.; Siraj, M. In-situ synthesis of $TiO_2/La_2O_2CO_3$/rGO composite under acidic/basic treatment with La^{3+}/Ti^{3+} as mediators for boosting photocatalytic H_2 evolution. *Int. J. Hydrogen Energy* **2019**, *44*, 23669–23688. [CrossRef]
32. Yin, H.; Cao, Y.; Fan, T.; Qiu, B.; Zhang, M.; Yao, J.; Li, P.; Liu, X.; Chen, S. Construction of carbon bridged TiO_2/CdS tandem Z-scheme heterojunctions toward efficient photocatalytic antibiotic degradation and Cr (VI) reduction. *J. Alloys Compd.* **2020**, *824*, 153915. [CrossRef]
33. Hossen, M.A.; Solayman, H.M.; Leong, K.H.; Sim, L.C.; Yaacof, N.; Abd Aziz, A.; Wu, L.; Monir, M.U. Recent progress in TiO_2-Based photocatalysts for conversion of CO_2 to hydrocarbon fuels: A systematic review. *Results Eng.* **2022**, *16*, 100795. [CrossRef]
34. Kim, S.H.; Lee, S.W.; Lee, G.M.; Lee, B.T.; Yun, S.T.; Kim, S.O. Monitoring of TiO_2-catalytic UV-LED photo-oxidation of cyanide contained in mine wastewater and leachate. *Chemosphere* **2016**, *143*, 106–114. [CrossRef] [PubMed]
35. Lv, K.; Fang, S.; Si, L.; Xia, Y.; Ho, W.; Li, M. Fabrication of TiO_2 nanorod assembly grafted rGO (rGO@TiO_2-NR) hybridized flake-like photocatalyst. *Appl. Surf. Sci.* **2017**, *391*, 218–227. [CrossRef]

36. Ge, M.; Li, Q.; Cao, C.; Huang, J.; Li, S.; Zhang, S.; Chen, Z.; Zhang, K.; Al-Deyab, S.S.; Lai, Y. One-dimensional TiO_2 Nanotube Photocatalysts for Solar Water Splitting. *Adv. Sci.* **2017**, *4*, 1600152. [CrossRef]
37. Soares, T.A.; Gonzalez-Moya, J.R.; Byun, Y.; Thesing, A.; Dares, C.; Coskun, A.; Machado, G. One-step anodization-electrophoretic deposition of titanium nanotubes-graphene nanoribbon framework for water oxidation. *J. Electroanal. Chem.* **2021**, *902*, 115802. [CrossRef]
38. Rajaitha, P.; Hajra, S.; Sahu, M.; Mistewicz, K.; Toroń, B.; Abolhassani, R.; Panda, S.; Mishra, Y.; Kim, H. Unraveling highly efficient nanomaterial photocatalyst for pollutant removal: A comprehensive review and future progress. *Mater. Today Chem.* **2022**, *23*, 100692. [CrossRef]
39. Rambabu, Y.; Jaiswal, M.; Roy, S.C. Enhanced photoelectrochemical performance of multi-leg TiO_2 nanotubes through efficient light harvesting. *J. Phys. D Appl. Phys.* **2015**, *48*, 295302. [CrossRef]
40. Rodríguez-Lazcano, Y.; Barrios-Salgado, E.; Flores-Castañeda, M.; Camacho-López, S.; Pérez-Alvarez, J.; Chávez-Chávez, A.; Quiñones-Galván, J.G. Physical properties of Sb_2S_3–Cu nanocomposite thin films synthesized by chemical bath deposition and laser ablation of solids in liquids. *J. Mater. Res. Technol.* **2023**, *24*, 6604–6613. [CrossRef]
41. Sahnesarayi, M.K.; Rastegari, S.; Sarpoolaky, H. Enhanced photoelectrochemical water splitting performance of vertically aligned Bi_2O_3 nanosheet arrays derived from chemical bath deposition method by controlling chemical bath temperature and complexing agent concentration. *Surf. Interfaces* **2022**, *30*, 101819. [CrossRef]
42. Qian, T.; Yin, X.; Li, J.; Xu, H.; Deng, Y.; Wang, X. Nano-TiO_2 Decorated Radial-Like Mesoporous Silica: Preparation, Characterization, and Adsorption-Photodegradation Behavior. *J. Mater. Sci. Technol.* **2017**, *33*, 1314–1322. [CrossRef]
43. Tichapondwa, S.M.; Newman, J.P.; Kubheka, O. Effect of TiO_2 phase on the photocatalytic degradation of methylene blue dye. *Phys. Chem. Earth Parts A/B/C* **2020**, *118–119*, 102900. [CrossRef]
44. Sun, T.; Zhao, Z.; Liang, Z.; Liu, J.; Shi, W.; Cui, F. Efficient degradation of p-arsanilic acid with arsenic adsorption by magnetic CuO-Fe_3O_4 nanoparticles under visible light irradiation. *Chem. Eng. J.* **2018**, *334*, 1527–1536. [CrossRef]
45. Xu, J.; Shen, X.; Wang, D.; Zhao, C.; Liu, Z.; Pozdnyakov, I.P.; Wu, F.; Xia, J. Kinetics and mechanisms of pH-dependent direct photolysis of p-arsanilic acid under UV-C light. *Chem. Eng. J.* **2018**, *336*, 334–341. [CrossRef]
46. Eldoma, M.A.; Alaswad, S.O.; Mahmoud, M.A.; Qudsieh, I.Y.; Hassan, M.; Bakather, O.Y.; Elawadi, G.A.; Abouatiaa, A.F.; Alomar, M.S.; Elhassan, M.S.; et al. Enhancing photocatalytic performance of Co-TiO_2 and Mo-TiO_2-based catalysts through defect engineering and doping: A study on the degradation of organic pollutants under UV light. *J. Photochem. Photobiol. A Chem.* **2024**, *446*, 115164. [CrossRef]
47. Wang, Y.; He, D.; Chen, H.; Wang, D. Catalysts in electro-, photo- and photoelectrocatalytic CO_2 reduction reactions. *J. Photochem. Photobiol. C Photochem. Rev.* **2019**, *40*, 117–149. [CrossRef]
48. Kocijan, M.; Ćurković, L.; Vengust, D.; Radošević, T.; Shvalya, V.; Gonçalves, G.; Podlogar, M. Synergistic Remediation of Organic Dye by Titanium Dioxide/Reduced Graphene Oxide Nanocomposite. *Molecules* **2023**, *28*, 7326. [CrossRef] [PubMed]
49. Wang, Z.; Li, Y.; Zhang, C.; Wu, J.; Cui, K.; Li, Q. Degradation of AO7 through RGO/TiO_2 nanotube arrays photoanode in UV/electrical coupling system: Performance and mechanism analysis. *Opt. Mater.* **2024**, *149*, 115030. [CrossRef]
50. Liu, K.; Zhao, L.; Yue, X.; Li, B.; Qin, X.; Li, Q.; Zhang, J. One-pot synthesis of CdS nanoparticles with surface-phase junctions to catalyze the photo-reduction of CO_2 into CO and CH_4 selectively. *Mater. Today Commun.* **2023**, *37*, 107205. [CrossRef]
51. Kalita, L.; Soni, A.; Kalita, S.J.; Basyach, P.; Guha, A.K.; Jain, S.L.; Saikia, L. Synergistic CdS@CeO_2 nanocomposites: Harnessing Z-scheme electron transfer for enhanced photocatalytic CO_2 conversion and aqueous Cr(VI) reduction. *J. Environ. Chem. Eng.* **2024**, *12*, 112930. [CrossRef]
52. Guo, Y.; Sui, M.; Liu, S.; Li, T.; Lv, X.; Yu, M.; Mo, Y. Insight into cobalt substitution in $LaFeO_3$-based catalyst for enhanced activation of peracetic acid: Reactive species and catalytic mechanism. *J. Hazard. Mater.* **2024**, *461*, 132662. [CrossRef]
53. Yadav, I.; Dutta, S.; Pandey, A.; Yadav, N.; Goyal, A.; Chatterjee, R. Evolution of TiOx-SiOx nano-composite during annealing of ultrathin titanium oxide films on Si substrate. *Ceram. Int.* **2020**, *46*, 19935–19941. [CrossRef]
54. Kozakov, A.; Kochur, A.; Kumar, N.; Panda, K.; Nikolskii, A.; Sidashov, A. Determination of sp2 and sp3 phase fractions on the surface of diamond films from C1s, valence band X-ray photoelectron spectra and CKVV X-ray-excited Auger spectra. *Appl. Surf. Sci.* **2021**, *536*, 147807. [CrossRef]
55. Caloudova, H.; Blahova, J.; Mares, J.; Richtera, L.; Franc, A.; Garajova, M.; Tichy, F.; Lenz, J.; Caloudova, J.; Enevova, V.; et al. The effects of dietary exposure to Magneli phase titanium suboxide and titanium dioxide on rainbow trout (*Oncorhynchus mykiss*). *Chemosphere* **2022**, *293*, 133689. [CrossRef]
56. Ahluwalia, S.; Prakash, N.T.; Prakash, R.; Pal, B. Improved degradation of methyl orange dye using bio-co-catalyst Se nanoparticles impregnated ZnS photocatalyst under UV irradiation. *Chem. Eng. J.* **2016**, *306*, 1041–1048. [CrossRef]
57. Bergamonti, L.; Predieri, G.; Paz, Y.; Fornasini, L.; Lottici, P.; Bondioli, F. Enhanced self-cleaning properties of N-doped TiO_2 coating for Cultural Heritage. *Microchem. J.* **2017**, *133*, 1–12. [CrossRef]
58. Balarabe, B.Y.; Paria, S.; Keita, D.S.; Baraze, A.R.I.; Kalugendo, E.; Tetteh, G.N.T.; Meringo, M.M.; Oumarou, M.N.I. Enhanced UV-light active α-Bi_2O_3 nanoparticles for the removal of methyl orange and ciprofloxacin. *Inorg. Chem. Commun.* **2022**, *146*, 110204. [CrossRef]
59. Bakar, S.A.; Byzynski, G.; Ribeiro, C. Synergistic effect on the photocatalytic activity of N-doped TiO_2 nanorods synthesised by novel route with exposed (110) facet. *J. Alloys Compd.* **2016**, *666*, 38–49. [CrossRef]

60. Shah, R.K. Efficient photocatalytic degradation of methyl orange dye using facilely synthesized α-Fe_2O_3 nanoparticles. *Arab. J. Chem.* **2023**, *16*, 104444. [CrossRef]
61. Khan, R.; Hassan, M.S.; Jang, L.-W.; Yun, J.H.; Ahn, H.-K.; Khil, M.-S.; Lee, I.-H. Low-temperature synthesis of ZnO quantum dots for photocatalytic degradation of methyl orange dye under UV irradiation. *Ceram. Int.* **2014**, *40*, 14827–14831. [CrossRef]
62. Khan, R.; Hassan, M.S.; Cho, H.-S.; Polyakov, A.Y.; Khil, M.-S.; Lee, I.-H. Facile low-temperature synthesis of ZnO nanopyramid and its application to photocatalytic degradation of methyl orange dye under UV irradiation. *Mater. Lett.* **2014**, *133*, 224–227. [CrossRef]
63. Isai, K.A.; Shrivastava, V.S. Photocatalytic degradation of methylene blue using ZnO and 2%Fe–ZnO semiconductor nanomaterials synthesized by sol–gel method: A comparative study. *SN Appl. Sci.* **2019**, *1*, 1247. [CrossRef]
64. Kurniawan, T.A.; Mengting, Z.; Fu, D.; Yeap, S.K.; Othman, M.H.D.; Avtar, R.; Ouyang, T. Functionalizing TiO_2 with graphene oxide for enhancing photocatalytic degradation of methylene blue (MB) in contaminated wastewater. *J. Environ. Manag.* **2020**, *270*, 110871. [CrossRef] [PubMed]
65. Qamar, M.A.; Shahid, S.; Javed, M.; Iqbal, S.; Sher, M.; Akbar, M.B. Highly efficient g-C_3N_4/Cr-ZnO nanocomposites with superior photocatalytic and antibacterial activity. *J. Photochem. Photobiol. A Chem.* **2020**, *401*, 112776. [CrossRef]
66. Goyal, P.; Chakraborty, S.; Misra, S.K. Multifunctional Fe_3O_4-ZnO nanocomposites for environmental remediation applications. *Environ. Nanotechnol. Monit. Manag.* **2018**, *10*, 28–35. [CrossRef]
67. Zhang, J.; Zhang, X.; Dong, S.; Zhou, X.; Dong, S. N-doped carbon quantum dots/TiO_2 hybrid composites with enhanced visible light driven photocatalytic activity toward dye wastewater degradation and mechanism insight. *J. Photochem. Photobiol. A Chem.* **2016**, *325*, 104–110. [CrossRef]
68. Abu Bakar, S.; Ribeiro, C. An insight toward the photocatalytic activity of S doped 1-D TiO_2 nanorods prepared via novel route: As promising platform for environmental leap. *J. Mol. Catal. A Chem.* **2016**, *412*, 78–92. [CrossRef]
69. Sabouri, Z.; Akbari, A.; Hosseini, H.A.; Khatami, M.; Darroudi, M. Egg white-mediated green synthesis of NiO nanoparticles and study of their cytotoxicity and photocatalytic activity. *Polyhedron* **2020**, *178*, 114351. [CrossRef]